RSC Advances

This article can be cited before page numbers have been issued, to do this please use: S. Maiti, A. Pramanik and S. Mahanty, *RSC Adv.*, 2015, DOI: 10.1039/C5RA05514H.

ROYAL SOCIETY OF CHEMISTRY

www.rsc.org/advances

View Article Online
DOI: 10.1039/C5RA05514H

Journal Name

ARTICLE

Influence of Imidazolium-based Ionic Liquid Electrolytes on the Performance of Nano-structured MnO_2 Hollow Spheres as Electrochemical Supercapacitor

Received 00th January 20xx,
Accepted 00th January 20xx

DOI: 10.1039/x0xx00000x

www.rsc.org/

Sandipan Maiti, Atin Pramanik and Sourindra Mahanty*

Use of room temperature ionic liquids (ILs) as electrolyte with a wider potential window offers a scope for developing high energy density supercapacitors for efficient energy storage. In this work, a comparative study on the performance of nanostructured MnO_2 hollow spheres as electrochemical supercapacitor was made by fabricating activated carbon (AC) // MnO_2 asymmetric supercapacitor cells using imidazolium-based ILs as electrolytes. Mesoporous MnO_2 hollow spheres were synthesized through a simple low temperature (80°C) solvothermal method by reduction of $KMnO_4$ under acidic condition in presence of Cu_3(1,3,5 benzenetricarboxylate)$_2$ metal organic framework (MOF) in the precursor solution, which acts as the source of Cu^{2+} playing a crucial role for the formation of the hollow spheres. Four different ILs were investigated from combinations of two different cations [1-ethyl-3-methylimidazolium (EMI^+) and 1-butyl-3-methylimidazolium (BMI^+) and four different anions [hexaflurophosphate (PF_6^-), tetrafluoroborate (BF_4^-), trifluromethanesulfonate (Otf^-) and bis(trifluromethylsulfonyl)imide ($TFSI^-$)]. Influences of the physico-chemical properties such as ionic size, nucleophilicity, viscosity of the IL on the electrochemical properties are discussed. A high energy density of 163 $WhKg^{-1}$, which is comparable to the energy density of a lithium-ion battery, could be achieved with $EMIMBF_4$ as electrolyte. The present findings would help in further research for developing IL-based supercapacitors.

Introduction

Electrochemical supercapacitors, that can bridge the energy/power gap between batteries and conventional dielectric capacitors, are being evolved as very important energy storage devices during the last few years for applications in mobile electronics, backup power supplies and have become an integral part in advanced hybrid/electric vehicles.[1-5] Conventional electrochemical double layer supercapacitors (EDLC) using high surface area carbon in various forms in aqueous electrolytes (e.g, KOH, Na_2SO_4 etc.) or organic electrolytes (e.g., a lithium salt like $LiPF_6$ dissolved in organic solvents like ethylene carbonate, dimethyl carbonate, propylene carbonate etc.) can offer only a low energy density.[6-8] While high energy densities of 120-200 $Whkg^{-1}$ can be achieved with modern lithium-ion batteries, the energy densities of present commercial supercapacitors stay at 5-10 $Whkg^{-1}$ level though with a higher power density, excellent cycle life and capacity retention.[9] Thus, present day EDLCs can compensate for the low power performance of lithium-ion battery (LIB) for high end applications, only when used in tandem. However, higher energy storage can be realized in pseudocapacitors where there is also a faradic component involved through charge transfer between active electrode material (a metal oxide for example) and electrolyte via surface adsorption, redox reaction and/or intercalation of ions.[10] Among various metal oxides, MnO_2 has long been recognized as one of the most promising pseudo-capacitive materials with many favourable attributes such as abundance, low cost and good electrochemical performance.[11] Therefore, a number of studies are focused on developing MnO_2 based pseducapacitors in aquous electrolytes as well as nonaquous electrolytes. Using MnO_2 nanostructures in aquous electrolyte, specific capacitance values of 140-279 Fg^{-1} have been reported.[12-14] Further improvements have been achieved by overcoming the intrinsic low conductivity issue through development of composite materials like MnO_2/graphene,[15-19] MnO_2/carbon nanotube (CNT),[20-22] and conductive polymer-based MnO_2-polyaniline (PANI),[23] or MnO_2-poly(3,4-ethylenedioxythiophene) (PEDOT),[24] and capacitance as high as 1068 Fg^{-1} has been realized. However, the energy density is still low as the operating voltage in aqueous electrolytes is limited to ~1.0 V. The energy density (E) and power density (P) of a two electrode supercapacitor are determined using the following equations:[25]

$$E = \frac{Cs \times (\Delta V)^2}{8} \qquad (1)$$

$$P = \frac{(\Delta V)^2}{4R} \qquad (2)$$

Fuel Cell & Battery Division, CSIR-Central Glass & Ceramic Research Institute, Kolkata 700032 and CSIR-Network Institutes for Solar Energy (NISE), India.
Email: mahanty@cgcri.res.in; s_mahanty@hotmail.com
Tel: +91-33-2322 3495 Fax: +91-33-2473 0957.
†Electronic Supplementary Information (ESI) available: A comparative performance table for metal oxide supercapacitors in ionic liquids, Impedance data. See DOI: 10.1039/x0xx00000x

View Article Online
DOI: 10.1039/C5RA05514H

where C_s is specific capacitance, ΔV is the discharge potential window and R is the equivalent series resistance. Obviously, the higher is the potential window of the electrolyte, the higher energy and power density is expected, though ionic concentration, mobility and breakdown voltage of the electrolyte may also limit the achievable energy density. Therefore, several work have been focused at developing MnO_2 supercapacitors in organic electrolytes where the operating voltage could be extended to 3V.[26-27] In 1 M $LiPF_6$ in PC/DMC, a maximum capacitance of 414 Fg^{-1} was obtained at a current density of 0.5 Ag^{-1} for a MnO_2//MnO_2 symmetric cell.[26] Ionic liquids (IL), with a wide potential window, are good candidates for their unique physico-chemical properties such as high thermal stability, negligible vapour pressure (i.e., neither flammable nor volatile), relatively high ionic conductivity and good thermal and electrochemical stability.[28-37] ILs are considered "task specific" as their properties can be tuned to suit a particular application taking advantage of the weak interaction between its constituents i.e., a large cation and a charge-delocalized anion.[38] Therefore, a suitable combination of a metal oxide (e.g., MnO_2) having high pseudocapacitance as electrode and a suitable IL with a large operational potential window (2-4 V) could result in a significant increase in the overall energy density. Rochefort et al.[39] first proposed faradic redox reactions of RuO_2 in α-picoline:trifluoroacetic acid (P-TFA), a protic IL, proposing involvement of protons. Since then several studies are devoted to develop metal oxide supercapactors by using both protic and aprotic IL based on their ionic nature, conductivity and durability.[40-43] (see Table-I, $ESI^{\dagger}$) Nevertheless, practical applications of ILs still seem difficult as a number of limitations such as high viscosity and poor wettability with electroactive materials are yet to be overcome. In this respect, chemical compatibility between the electrode material and the IL electrolyte is also an important issue.

As the electrical double layer (EDL) structure in ILs would be different, a charge storage mechanism based on a double-injection process, involving the reversible uptake of small cations (for example, H^+, Li^+, Na^+, or K^+) and electrons cannot be applied for aprotic IL. Thus, for a given electrode material e.g., MnO_2, the double layer capacitance, interfacial tension and surface charge density would vary from IL to IL and ultimately influence the interfacial processes. There are a number of recent studies on the capacitive performances of MnO_2 in IL electrolytes.[10, 44-47] These studies have shown that though the voltage window could be extended up to 3 V, the specific capacitance obtained (~100 Fg^{-1}) are generally low. Recently, by modifying MnO_2 with metallic gold and high surface area carbon, Zhang et al.[47] have obtained a capacitance of ~523 Fg^{-1} at a current density of 3 Ag^{-1} for a NF/CNT/Au/MnO_2//AC hybrid asymmetric cell in 1-butyl-3-methyl-imidazolium hexafluorophosphate in DMF. That the observed capacitance values are lower in IL compared to those in aqueous electrolytes might have resulted from partial redox reactions due to poor ion insertion, limiting the faradic reduction and oxidation reactions.[10] Also, variation in the geometric shape of the constituent ions in different ILs may lead to the different interactions with MnO_2 affecting the resulting pseudocapacitive performance.[48] Therefore, it appears that despite the progress made, more work in this area is necessary to understand and rationalize the behaviour of different ILs for improving the charge storage abilitiy of MnO_2.

It is well known that capacitance is directly related to active surface area and pore-size distribution of the electrode material for easy access of the electrolyte.[49] Therefore, optimization of the electrode material is equally important as the optimization of the electrolyte for achieving energy and power densities closer to the theoretical limits of supercapacitors. It has been realised that design of nanostructured electrode materials with controlled mesopores is a critical aspect to reach a compromise between these two important parameters. Particularly, 3D hierarchical porous nanostructures with a spherical morphology provide the best performance.[50]

In the present work, we have synthesized hierarchically mesoporous 3D hollow spheres of MnO_2 by a modified solvothermal method in presence of Cu^{2+} ion and applied it to investigate the comparative performance of four different aprotic ILs as electrolytes in asymmetric hybrid activated carbon (AC)//MnO_2 supercapacitors. IL families with imidazolium cations are considered for a broad range of applications including electrochemical supercapacitors for their high mobility and a wide potential window.[10, 47, 51-59] In order to make a systematic study, we have chosen four imidazolium based ILs namely, 1-butyl-3-methylimidazolium hexaflurophosphate [BMIMPF$_6$] in DMF, 1-ethyl-3-methylimidazolium bis(trifluromethylsulfonyl)imide [EMIMTFSI), 1-ethyl-3-methylimidazolium tetrafluoroborate [EMIMBF$_4$] and 1-butyl-3-methylimidazolium triflurometh anesulfonate [BMIMOtf] which would allow us to compare combinations of two different cations [1-ethyl-3-methylimidazolium (EMI^+) and 1-butyl-3-methylimidazolium (BMI^+)] and four different anions [hexaflurophosphate (PF_6^-), tetrafluoroborate (BF_4^-), triflurometh anesulfonate (Otf^-) and bis(trifluromethylsulfonyl)imide (TFSI)]. We show here that the physico-chemical properties of the ILs and the constituent ions strongly influence the electrochemical performance and a high energy density of 163 $WhKg^{-1}$, which is comparable to the energy density of a lithium-ion battery, could be achieved with EMIMBF$_4$ as electrolyte.

Experimental

Synthesis of nanostructured MnO_2. Ultrapure water, obtained from a three-stage Millipore Mill-Q (Merck, Germany) purification system, was used in all experiments.

Hollow spherical nanostructured MnO_2 was prepared by low temperature solvothermal method under acidic condition. In a typical synthesis, 1.69 g (11 mmol.) of $MnSO_4.H_2O$ (99+%, Acros organics, India) was dissolved in 100 ml of deionized water, and 0.5 gm of Cu_3(1,3,5-benzenetricarboxylate)$_2$ MOF (Cu-BTC) was added to the solution as a source of Cu^{2+}. Then 1.0 ml of concentrated H_2SO_4 and 1.043 g (6.6 mmol.) of

View Article Online
DOI: 10.1039/C5RA05514H

$KMnO_4$ (99+%, Merck, Germany) dissolved in 66 ml deionized water, were simultaneously added drop-wise to the solution with constant stirring. The mixture was then transferred to a 500 ml sealed glass bottle and kept on a hot plate maintaining the temperature at 80°C for 12 h. After that, it was allowed to cool to room temperature. The black mass obtained was centrifuged and washed several times with deionized water and absolute alcohol to remove residual reactants. Finally, the product was dried at 110°C for 12 h in a vacuum oven. For comparison, MnO_2 was also synthesized under the same reaction conditions without addition of Cu-BTC MOF.

1-ethyl-3-methylimidazolium tetrafluoroborate ($EMIMBF_4$) (>98%), 1-ethyl-3-methylimidazolium bis(trifluromethylsulfonyl)imide (EMIMTFSI) (99%) and 1-butyl-3-methylimidazolium trifluromethanesulfonate (BMIMOtf) (99%) were purchased from Reinste Nano Ventures Private Limited, India. 1-butyl-3-methylimidazolium hexaflurophosphate ($BMIMPF_6$) (98+%) and N,N-Dimethylformamide (DMF) (99%) were purchased from Acros Organics, Germany. All the ionic liquids were used in the as received form without any further treatment.

Activated carbon (AC) (carbon content >95%, ash content <0.07%) was purchased from MTI Corporation, USA).

Material characterization. X-ray powder diffractograms were recorded in the 2θ range 10°-80° at a scanning rate of 2° min^{-1} by an X-ray diffractometer (Philips X'Pert, The Netherlands) with a Cu- K_α radiation at 40 KV and 40 mA. Phase analyses of the X-ray diffraction profiles were carried out using PANalytical HighscorePlus program. Morphology and Microstructural features were examined by a field emission scanning electron microscope (ZEISS Supra 35, Germany) and a transmission electron microscope (TEM/HRTEM/SAED), Tecnai G^2 30ST (FEI) with an accelerating voltage of 300 kV. The synthesized MnO_2 nanorods were further characterized by a Renishaw In via Reflex micro Raman spectrometer using 488 nm line of an Ar^+ ion laser for excitation in the range 200-1500 cm^{-1}. Thermogravimetric analysis (TGA) was carried out under argon flow at a heating rate of 10°C min^{-1} using Simultaneous Thermal Analyzer (STA 449F, Netzsch, Germany). Nitrogen adsorption-desorption measurements were been carried out using a Quantachrome Autosorb surface analyzer at 77.3 K. The sample was degassed under vacuum at 200°C for 3 h prior to measurement. The specific surface area of MnO_2 was determined by nitrogen gas absorption through Brunauer-Emmett-Teller (BET) method. Pore size distribution was estimated from desorption isotherm by the Barrett-Joyner-Halenda (BJH) method. Pore volume was determined from the amount of nitrogen gas adsorbed at $P/P_0 = 0.98$.

Electrochemical measurements. The working electrodes were fabricated by mixing 80 wt% active material, 10 wt% SuperP carbon and 10 wt% polyvinylidene fluoride (PVDF) in N-methyl-2-pyrrolidone (NMP) to form a viscous slurry. The slurry was then casted on an Al-foil (thickness, 20μm). The electrodes were heated at 110°C for 6 h in a vacuum oven to evaporate the residual solvent. The electrodes were hot-pressed and cut into circular discs having a diameter of 15 mm. The activated carbon (AC) electrodes of similar dimensions were also prepared by following the same procedure using 90:10 weight ratio of AC:PVDF. Two-electrode asymmetric supercapacitor coin cells (2032 type) were assembled with a MnO_2 electrode and an AC electrode separated by a Celgard 2300 membrane (thickness 20 μm). The mass of the active materials on the respective electrodes were around ~1.2 mg for AC electrode and ~1.5 mg for MnO_2 electrode i.e. at a weight ratio of 0.8:1.0 (the accuracy of electronic balance, 0.01 mg; MS105DU, Mettler Toledo, USA). Cyclic voltammetry (CV), galvanostatic charge-discharge and AC electrochemical impedance spectroscopy (EIS) were carried out by a galvanostat-potentiostat (PGSTAT 300N, Autolab, the Netherlands). All the CVs were measured between 0.0-2.5 V or 0-3 V at different scan rates of 2, 5, 10, 20, 50 and 100 mVs^{-1}. Galvanostatic charge-discharge measurements were carried out at current densities of 0.2, 0.5, 1, 2 and 5 Ag^{-1} in the same potential window. EIS measurements were carried out in the frequency range of 0.1 Hz-1.0 MHz at open circuit potential with an AC amplitude of 10 mV and the obtained data were fitted to an equivalent circuit model using NOVA 1.9 software.

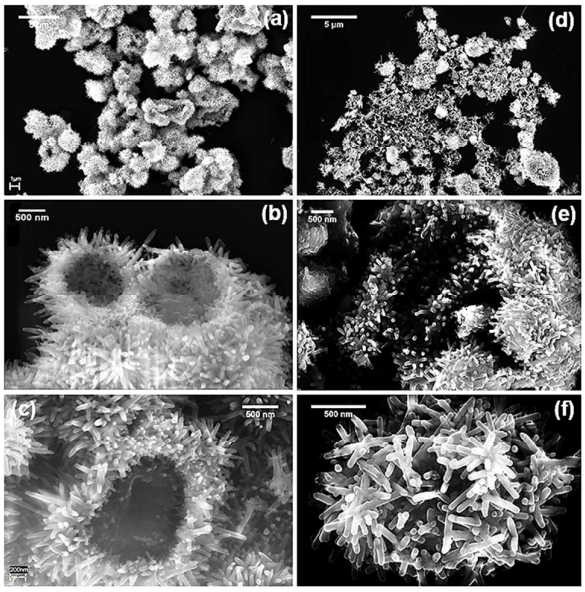

Fig.1 FESEM micrographs of MnO_2, solvothermally synthesized in presence of Cu-BTC MOF (a-c), and without Cu-BTC MOF (d-f)

Results and Discussion

Fig.1a-c shows the FESEM micrographs of MnO_2, synthesized in presence of Cu^{2+}, at different magnifications. The morphology consists of uniformly distributed microspheres of size ~1 μm in diameter. A closer look at a partially broken microsphere reveals that these are hollow in nature with a sea urchin like appearance and are composed of outwardly protruding interweaved nanorods having an average diameter of ~50 nm. The hollow cavity is clearly visible in a broken sphere as shown

View Article Online
DOI: 10.1039/C5RA05514H

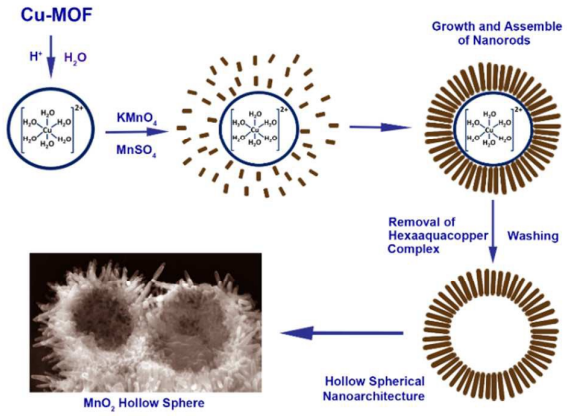

Scheme-1 A probable formation mechanism of MnO_2 hollow spheres

in Fig.1c. On the other hand, such kind of spheres with hollow cavity was not formed for MnO_2 when synthesized in absence of Cu-BTC. Instead, dispersed bundles of entangled nanorods of similar average diameter were resulted as revealed by the FESEM micrographs (Fig.1d-f). The role of Cu-BTC and a probable formation mechanism for the hollow spheres are depicted in Scheme-1. Cu-BTC MOF acts as a source of copper ions which play a key part. The metal ligand bonding in Cu-BTC being unstable under acidic condition, Cu^{2+} ions come out of the MOF to generate hexaaquacopper complex $[Cu(H_2O)_6]^{2+}$ on addition of H_2SO_4 into the reaction mixture. The hexaaquacopper complex, where water molecules are octahedrally coordinated around the Cu^{2+} ion forming a large positively charged species, acts as the nucleation site. The double chains of octahedral $[MnO_6]$ in 2x2 tunnels, which are the building blocks of MnO_2 structure, are grown from the very beginning of the reaction. In presence of positively charged $[Cu(H_2O)_6]^{2+}$, these MnO_6 in 2x2 tunnels orient themselves on the periphery of the large hexaaquacopper complex. Self-assembly occurs by weak interactions between these building blocks through Van der walls forces or hydrogen bonding.[60] Later on, with subsequent repeated washing with water, evacuation of $[Cu(H_2O)_6]^{2+}$ takes place through dissolution resulting in the formation of hollow cavity with conglomeration of radial nanorods.

TEM images, shown in Fig.2a-d, further confirm the hollow nature of the microspheres. The constituent nanorods are found to have sharp spike-like ends. The average diameter of the nanorods is estimated to be ~50 nm. The HRTEM image shows clear fringes with a spacing of 4.9Å, which agrees well with the interplanar distance of (200) planes of α-MnO_2. In the selected area diffraction pattern (Fig.2e), well-defined diffraction spots, arranged in circular rings, are observed confirming the formation of well-crystallised polycrystalline α-MnO_2 with characteristics planes clearly identified. HRTEM analysis reveal that the nanorods are growing along the [001] direction.

MnO_2 is known to exist in different polymorphic forms.[61-62] In order to examine the phase purity of the synthesized hollow

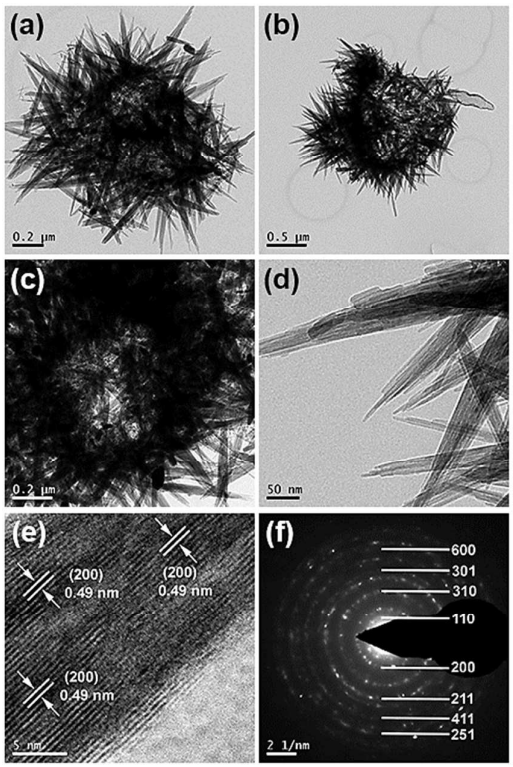

Fig.2 TEM images of synthesized MnO_2 at different magnifications (a-d), HRTEM image showing the lattice fringes (e), and the corresponding selected area diffraction pattern (f)

spheres, x-ray diffraction measurements were conducted. All the observed peaks in the diffractogram (Fig.3a) could be indexed to a tetragonal phase (space group: I4/m) of α-MnO_2 (JCPDS Data File No. 00-044-0141). The calculated lattice parameters are found to be a = b = 9.842 Å and c = 2.857 Å, which are in good agreement with values reported in literature.[63] No additional diffraction peak is observed

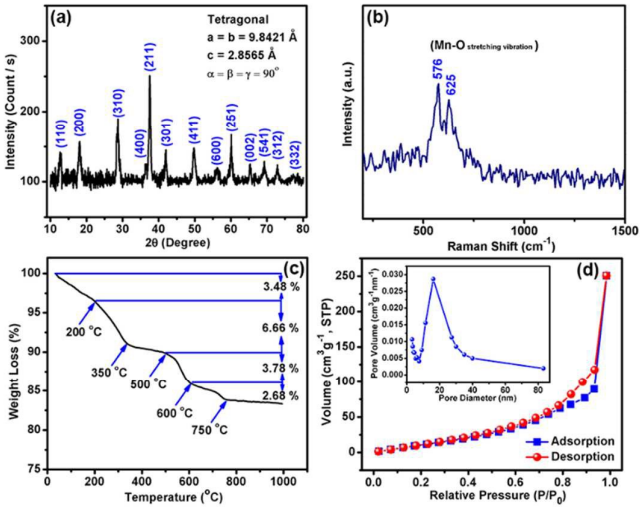

Fig.3 X-ray diffractogram (a), Raman spectrum (b), TGA plot (c), and adsorption-desorption isotherms (d) of synthesized MnO_2

View Article Online
DOI: 10.1039/C5RA05514H

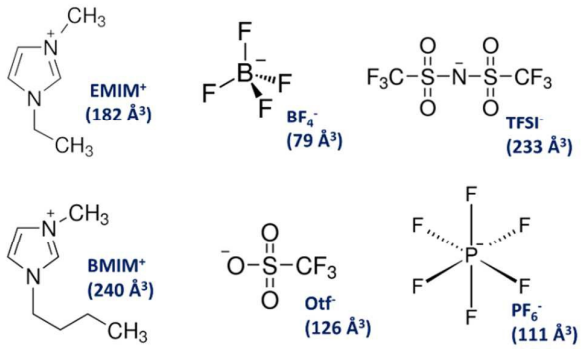

Fig.4 Schematic representation of the molecular structures of the constituent ions of the ILs. The respective ionic volumes are given in the parenthesis

indicating high purity of the synthesized single phase tetragonal α-MnO_2. The synthesized α-MnO_2 nanorods were further characterized by Raman spectroscopy. A strong band at 576 cm^{-1} is observed in the Raman spectrum (Fig.3b), which is characteristic of Mn-O lattice vibration in α-MnO_2.[64] However, an additional band is observed at 625 cm^{-1} which corresponds to Mn-O lattice vibration in Mn_3O_4. Appearance of this band can be assigned to the formation of Mn_3O_4 by local heating of α-MnO_2 nanorods during acquisition of the spectrum.[65-66]

Thermogravimetric analysis (Fig.3c) shows a series of successive weight losses, typical of α-MnO_2. The observed weight losses can be broadly divided into four steps. Initially, a small weight loss of ~3.5% occurs between 30-200°C due to the loss of physically absorbed water. A second weight loss of ~6.6% between 201-300°C can be assigned to loss of chemisorbed oxygen and water. Thereafter, no weight loss is observed till 500°C. Further weight loss of ~3.8% in the 500-600°C range represents detachment of lattice oxygen from manganese oxide,[67] and finally, about 2.7% weight in the 600-750°C range indicates thermal decomposition of the Mn(IV) oxide to a lower oxidation state of Mn with evolution of lattice oxygen. Thus, the results indicate that the synthesized MnO_2 is thermally stable up to 500°C.

Surface area, pore sizes and their distribution play a crucial role in determining the performance of a material as supercapacitor. Fig.3d shows the N_2 adsorption-desorption

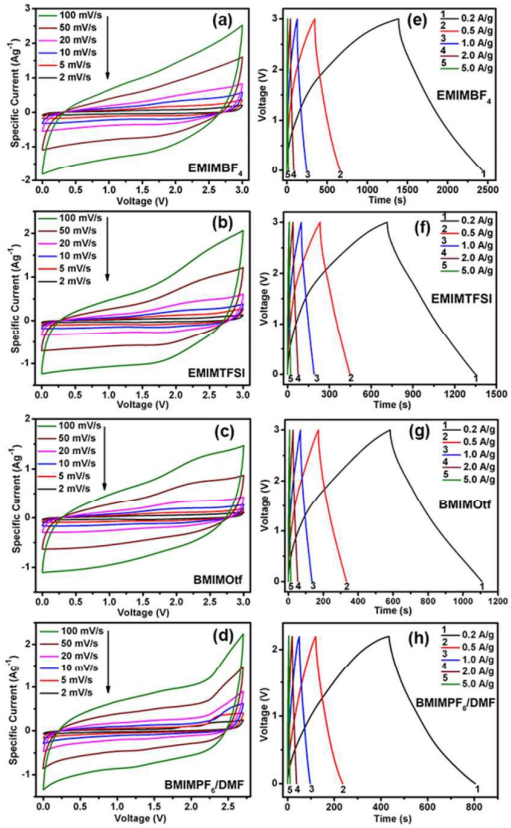

Fig.5 Electrochemical properties of AC//IL//MnO_2 assymmetric hybrid cells: cyclic voltammograms at different scan rates of 2-100 mVs^{-1} for different ILs (a-d), and respective galvanostatic charge discharge plots at different current densities of 0.2-5 Ag^{-1} (e-h)

isotherms of synthesized MnO_2 hollow spheres along with the pore size distribution plot in the inset. The configuration of the plot displays a typical type II/IV isotherm with a discrete hysteresis loop in the range P/P_0 = 0.5-0.95 which is indicative of the presence of a mesoporous structure in the cavities of the hollow spheres.[68] A gravimetric BET surface area of 85 m^2g^{-1} has been obtained. The pore size distribution, calculated from the adsorption part of the nitrogen sorption isotherm, reveals a broad size distribution in the range of 8-40 nm with

Table-I. The Physico-chemical Properties of ILs.

Ionic Liquids	Chemical Formula	Density (g cm^{-3})	Viscosity (cP)	Thermal Decomposition Temperature (°C)	Specific Conductivity [S m^{-1}]
1-ethyl-3-methylimidazolium tetrafluoroborate ($EMIMBF_4$)	$C_6H_{11}BF_4N_2$	1.294	26	>350	0.15
1-ethyl-3-methylimidazolium bis(trifluromethylsulfonyl)imide (EMIMTFSI)	$C_8H_{11}F_6N_3O_4S_2$	1.52	34	455	0.88
1-butyl-3-methylimidazolium triflate (BMIMOtf)	$C_9H_{15}F_3N_2O_3S$	1.292	179	409	0.37
1-butyl-3-methylimidazolium hexaflurophosphate ($BMIMPF_6$)	$C_8H_{15}F_6N_2P$	1.37	284	>350	0.22

View Article Online
DOI: 10.1039/C5RA05514H

an average pore size of ~16 nm. Existence of such large sized pores would provide easy access to the large IL molecules/ions and the high surface area would increase the number of available active sites.

Schematic molecular structures of the constituent cations and anions of the four imidazolium based ILs are shown in Fig.4. The relevant physical properties of the ILs are also given in Table-I. Following the best practice method,[69] the electrochemical properties of the synthesized MnO_2 hollow spheres as supercapacitor have been investigated in two-electrode configuration by assembling asymmetric AC//IL//MnO_2 cells. Fig.5a-d shows cyclic voltammograms of the supercapacitor cells recorded at different scan rates of 2, 5, 10, 20, 50 and 100 mVs^{-1} using four different ILs as electrolytes. While $EMIMBF_4$, EMIMTFSI and BMIMOtf could operate at a relatively higher potential window of 0-3.0 V, the potential window was limited to 0.0-2.5 V for $BMIMPF_6$ beyond which large irreversible current results. This could be due to the fact that PF_6^-, being a non-coordinating anion with poor nucleophilicity, is prone to decomposition of the IL. However, it is observed that in each of these ILs, the asymmetric capacitors show a near rectangular shaped voltammograms, typical of MnO_2 in two-electrode configuration,[10, 44-47] indicating good capacitive properties. As the scan rate is increased from 2 mVs^{-1} to 100 mVs^{-1}, the rectangular shape is somewhat distorted; a feature which is commonly observed for pseudocapacitors. Irregular shapes in CV may also appear due to differences in the sizes of cation and anion of ILs, suggesting that with a suitable matching of pores size of the electrode material (MnO_2 in this case) further improvement could be possible. The charge storage mechanism in these AC//MnO_2 cells is of a mixed type containing both EDLC (non-faradic ion adsorption/desorption on the surface of MnO_2) and pseudocapacitive (faradic ion diffusion into the bulk MnO_2) characteristics. This is also reflected by appearance of broad redox peaks between 1.5 and 2.2 V, particularly at higher scan rates. The corresponding galvanostatic charge-discharge (GCD) profiles at different current densities of 0.2, 0.5, 1, 2 and 5 Ag^{-1} are shown in Fig.5e-h. A near triangular shaped GCD, as observed for each of the ILs at all current densities is indicative of smooth charge propagation across the two electrodes, characteristics of a good electrochemical capacitor. This is further highlighted by observance of only a small IR drop at the beginning of the discharge curve indicating low equivalent series resistance (ESR) of the cells.[70] Slightly unsymmetrical nature the charge and discharge plots and a small deviation from linearity are resulted from the faradic component involving redox processes. Specific capacitance (C_s) values were calculated from the discharge profile using the equation:

$$Cs = \frac{4\times I\times \Delta t}{\Delta V\times m} \qquad (3)$$

where, m represents the sum of the total active mass of both electrodes. While calculating C_s, the voltage values were corrected for the Ohmic drop. A comparison of C_s obtained in

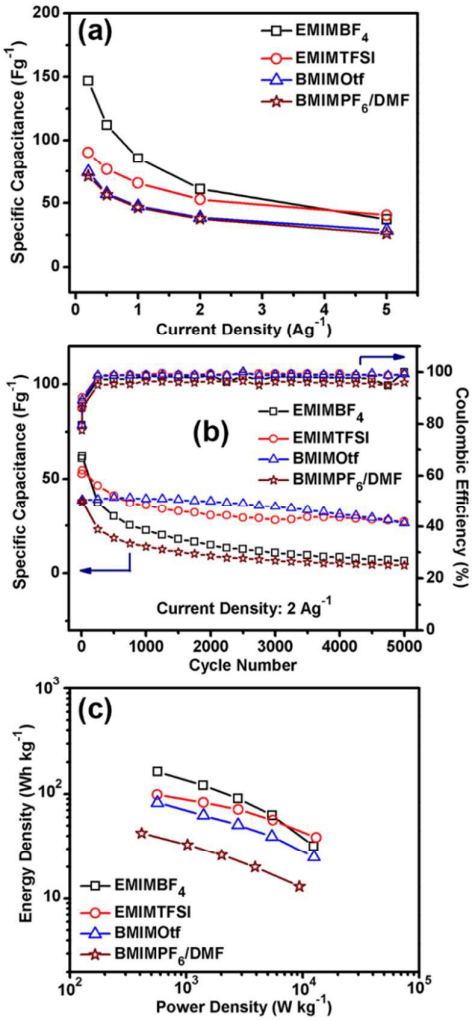

Fig.6. Electrochemical properties of AC//IL//MnO_2 assymmetric hybrid cells: variation in specific capacitance with current density (a), cycling performance (b), and Ragone plots (c)

different ILs shows that at a lower current density of 0.2 Ag^{-1}, the order of specific capacitance is $EMIMBF_4$ > EMIMTFSI > BMIMOtf > $BMIMPF_6$ with values of 147, 90.3, 74.4 and 71.3 Fg^{-1} respectively. Li et al.[45] has proposed that the pseducapacitive charge storage mechanism of MnO_2 in IL is generally dominated by the anions because the cations used (such as imidazolium) are too large to get involved in the insertion/de-insertion process compensating the Mn^{3+}-Mn^{4+} valence change. Chen et al.[10] have related the performance of ILs to the intrinsic interactions between MnO_2 and the organic molecules where the relative position of the highest occupied molecular orbital (HOMO) of the IL and the Fermi level of MnO_2 determines the efficacy of the charge transfer process. While these may be probable, the dimension of the cation and the physico-chemical properties of ILs would still play a very significant role affecting ion transport to the electrode surface sites via possible formation of ionic clusters, particularly for asymmetric cells with AC as an electrode where there might be

View Article Online
DOI: 10.1039/C5RA05514H

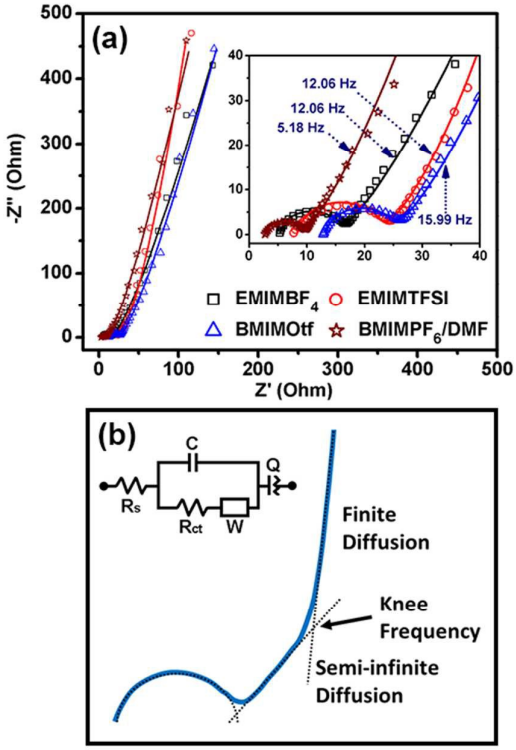

Fig.7 Electrochemical impedance spectra of AC//IL//MnO_2 assymmetric hybrid cells (a) and the equivalent circuit model (b)

a considerable EDLC component involved. [BMI^+] having a longer side chain than [EMI^+] imparting larger cation volume would result in a reduced concentration of ions at the electrode-electrolyte interface. Between $EMIMBF_4$ and EMIMTFSI, the former has a lower viscosity and higher specific conductivity. Also, the ionic radius of BF_4^- is less than $TSFI^-$. Therefore, $EMIMBF_4$ shows the highest Cs (147 Fg^{-1}) amongst all four ILs studied. On the other hand, between BMIMOtf and $BMIMPF_6$, a high viscosity of the later results in a low value of Cs (71.3 Fg^{-1}). Also, the hierarchical mesoporous nature and high surface area of MnO2 hollowspheres would lead to enhanced EDLC behaviours. The macropores & mesopores would provide easy pathways for the electrolyte ions to access every available surface and the microporous walls would strengthen the electrical double layer capacitance.

Rate performance of the asymmetric supercapacitors has been tested at current densities of 0.2, 0.5, 1, 2 and 5 Ag^{-1} and is shown in Fig.6a. As the current density increases, the specific capacitance decreases in all four ILs. However, it is observed that the decrease in capacitance is more prominent in case of [EMI^+] containing ILs (EMIMTFSI and $EMIMBF_4$) than in case of [BMI^+] containing BMIMOtf and $BMIMPF_6$. Also, BF_4^- being a poor nucleophile compared to TFSI, a sharper decrease in C_s is observed. At a high current density of 5 Ag^{-1}, the specific capacitance values of 37.2, 40.4, 28.6 and 26 Fg^{-1} are obtained for $EMIMBF_4$, EMIMTFSI, BMIMOtf and $BMIMPF_6$ respectively. Such relatively poor rate performance is generally observed for MnO_2 in the pristine form and can be assigned to its intrinsic low electronic conductivity.[71]

Long cycle life is marked as a characteristic of a supercapacitor. In order to access the cycling performances, the cells have been subjected to 5000 continuous charge discharge cycles at a current density of 2 Ag^{-1} and the results are shown as plots of cycle number vs specific capacitance in Fig.6b. It is observed that BMIMOtf and EMIMTFSI show relatively stable performance with 68 and 52% of retention of capacity after 5000 cycles. On the other hand, $EMIMBF_4$ and $BMIMPF_6$ show a poor cycling performance with only retention of ~ 11% of the original capacity. The results indicate that not only the size, nucleophilicity of the anions also plays a significant role. Here, both BF_4^- and PF_6^- being poor nucleophiles, have lesser coordinating ability and interact only weakly with the cations. Thus, $EMIMBF_4$ and $BMIMPF_6$ are more susceptible for decomposition during prolonged cycling.

Energy density (E) and power density (P) are the parameters which are usually used to evaluate the performance of electrochemical supercapacitors.[72] For a high performance supercapacitor, a reasonable energy density is required with a high power density. Fig.6c shows the Ragone plots obtained from the GCD data, which gives a measure of the available energy of the cells for constant active power request. It can be observed that a high energy density of 163 $Whkg^{-1}$ could be obtained for $EMIMBF_4$ at a power density of ~600 Wkg^{-1}. At similar power densities, the corresponding energy density values are 99, 83 and 43 $Whkg^{-1}$ for EMIMTFSI, BMIMOtf and $BMIMPF_6$ respectively. However, with the increase in power density, a gradual decrease in energy density value is observed. At power densities > 10 $kWKg^{-1}$, about 25, 45, 38 and 36% of capacitance are obtained for $EMIMBF_4$, EMIMTFSI, BMIMOtf and $BMIMPF_6$ respectively with respect to the corresponding energy density obtained at ~600 Wkg^{-1}. As discussed earlier, this can partly be attributed to the low electrical conductivity of MnO_2. The results show that $EMIM^+$ containing ILs deliver higher energy density at all power densities compared to $BMIM^+$ containing ILs. It is known that the viscosity and conductivity of ILs would adversely influence the energy/power density of the device.[73] $BMIM^+$ ILs having a larger ionic volume and higher viscosity compared to $EMIM^+$ ILs results in a poorer performance. On the other hand, relatively poor retention in $EMIMBF_4$ and $BMIMPF_6$ can be related to the poor nucleophilicity of BF_4^- and PF_6^- anions. Nevertheless, the observed energy density of 163 $Whkg^{-1}$, obtained for $EMIMBF_4$, is quite high for IL based supercapacitors and even comparable to the energy density of lithium-ion batteries.[9] Further, it might be possible that the energy and power density can still be improved for $EMIMBF_4$ through the balancing of active masses of the electrodes in the asymmetric AC//MnO_2 cell and also by improving the electrical conductivity of the MnO_2 though designing a suitable carbon based composite electrode. Although the ionic liquid has a viscosity higher than aqueous and organic electrolytes, the cells are still capable of delivering reasonable energy density at high power densities due to the mesoporous structure of synthesized MnO_2.

View Article Online
DOI: 10.1039/C5RA05514H

Electrochemical impedance spectroscopy (EIS) is an important tool for analyzing the performance of supercapactor cells. Fig.7a shows the Nyquist plots obtained for the cells using four ILs in as assembled states. The equivalent circuit model used to fit impedance data and a schematic model for estimation of the 'knee frequency' is shown in Fig.7b (for fitted data see Table-II, ESI†). The intercept on the real axis (Z') in the high frequency region represents the internal resistance (R_s) of the cell which is a combination of the intrinsic resistance of electrode material, ionic resistance of the electrolyte and contact resistance between electrode and current collector. Despite the ILs being viscous with relatively low specific conductivity, R_s values are found to be low (3.0-13.4 Ω). A semicircle, observed at the intermediate frequency region, originates the faradic pseudo-capacitance,[74] the diameter of which resembles to the charge transfer resistance (R_{ct}). Low R_{ct} values (5.8-13.9 Ω) indicate good charge transfer ability of the developed hierarchically porous MnO_2 electrode in all four ILs. A straight line at an angle ~45° observed at the intermediate frequency is related to Warburg resistance (W) which is related to the ionic diffusion in the electrolyte/electrode interface. While W values for $EMIMBF_4$, EMIMTFSI and BMIMOtf are relatively low (8.5-9.2 Ω), a higher value of 15.6 Ω) for $BMIMPF_6$ indicates poorer ionic diffusion. In the low frequency region, an almost vertical spike was observed which tends to be parallel to the Y-axis symbolizing a prominent capacitive behaviour.[75] A deviation from 90° may have resulted from the porous nature of the MnO_2 electrode and/or due to the low conductivity of the ILs.[73] A constant phase element, Q, representing the limiting capacitance, corresponds to the spike region of the Nyquist plot. The "knee" frequency (Fig.7b) where the impedance of the electrode starts to be dominated by capacitive behavior reflects the highest frequency where most of the capacitance is retained.[76-77] The active ions in the IL undergo semi-infinite diffusion at frequencies higher than the knee frequency and finite diffusion at frequencies below the knee frequency. Therefore, a high knee frequency is a signature of a good electrochemical capacitor.[77-78] Knee frequency values of 12.06, 12.06, 15.99 and 5.18 Hz have been observed for $EMIMBF_4$, EMIMTFSI, BMIMOtf and $BMIMPF_6$. As the knee frequency is related to the diffusion coefficient and effective diffusion length of the active material, MnO_2 in this case with the same diffusion coefficient, the observed slight differences can be assigned to the increase in the effective diffusion length due to differences in the ionic sizes of the ILs.[79]

Conclusions

In summary, herein we have demonstrated formation of nanostructured MnO_2 hollow spheres through a simple Cu^{2+} mediated solvothermal process. A comparative study of the performance of MnO_2//AC as electrochemical supercapacitor in four imidazolium based RTILs shows that chemical compatibility, physico-chemical characteristics and sizes of the constituent ions of ILs are the determining factors. Both cation and anion play important roles. $EMIM^+$ containing ILs are found to be better performing than $BMIM^+$ containing ILs. Best performance was achieved with $EMIMBF_4$ with a capacitance of 147 Fg^{-1} and an energy density of 163 $WhKg^{-1}$. Such high values could partly be attributed to the unique porous structure of the high surface area MnO_2 hollow spheres where the mesopores enables the IL ions to get access and wet electrode surface for efficient ion transport. Further improvement might be possible by improving the electrical conductivity of MnO_2 through formation of a suitable composite containing a conducting matrix. The present work will help in the ongoing quest for a compatible IL towards developing high energy density electrochemical supercapacitors.

Acknowledgements

The authors thank Director, CSIR-CGCRI for kind permission to publish this work. Financial support from CSIR via TAPSUN NWP0056 project is gratefully acknowledged.

Notes and references

1 M. Winter and R. J. Brodd, *Chem. Rev.*, 2004, **104**, 4245-4269.
2 B. E. Conway, *J. Electrochem. Soc.*, 1991, **138**, 1539-1548.
3 J. Yan, Z. Fan, T. Wei, W. Qian, M. Zhang, F. Wei, *Carbon*, **2010** 48, 3825-3833.
4 X. Wang, Y. Y. Wang, C. M. Zhao, Y. X. Zhao, B. Y. Yan and W. T. Zheng, *New J. Chem.*, 2012, **36**, 1902-1906.
5 R. S. Hastak, P. Sivaraman, D. D. Potphode, K. Shashidhara and A. B. Samui, *Electrochim. Acta*, 2012, **59**, 296-303.
6 Y. Tan, C. Xu, G. Chen, Z. Liu, M. Ma, Q. Xie, N. Zheng and S. Yao, *ACS Appl. Mater. Interfaces*, 2013, **5**, 2241-2248.
7 B. You, J. Jiang and S. Fan, *ACS Appl. Mater. Interfaces*, 2014, **6**, 15302-15308.
8 M. G. Hahm, A. L. M. Reddy, D. P. Cole, M. Rivera, J. A. Vento, J. Nam, H. Y. Jung, Y. L. Kim, N. T. Narayanan, D. P. Hashim, C. Galande, Y. J. Jung, M. Bundy, S. Karna, P. M. Ajayan and R. Vajtai, *Nano Lett.*, 2012, **12**, 5616-5621.
9 Y. Hou, L. Chen, P. Liu, J. Kang, T. Fujita and M. Chen, *J. Mater. Chem. A*, 2014, **2**, 10910-10916.
10 L. Y. Chen, J. L. Kang, Y. Hou, P. Liu, T. Fujita, A. Hirata and M. W. Chen, *J. Mater. Chem. A*, 2013, **1**, 9202-9207.
11 H. Lee and J. B. Goodenough, *J. Solid State Chem.*, 1999, **144**, 220-223.
12 H. Jiang, T. Zhao, J. Ma, C. Yan and C. Li, *Chem. Commun.*, 2011, **47**, 1264-1266.
13 D.-Y. Sung, I. Y. Kim, T. W. Kim, M.-S. Song and S.-J. Hwang, *J. Phys. Chem. C*, 2011, **115**, 13171-13179.
14 M.-S. Song, K. M. Lee, Y. R. Lee, T. W. Kim, S.-J. Hwang, *J. Phys. Chem. C*, 2010, **114**, 22134-22140.
15 S. Deng, D. Sun, C. H. Wu, H. Wang, J. B. Liu, Y. X. Sun and H. Yan, *Electrochim. Acta*, 2013, **111**, 707-712.
16 H. Gao, F. Xiao, C. B. Ching and H. Duan, *ACS Appl. Mater. Interfaces*, 2012, **4**, 2801-2810.
17 G. Yu, L. Hu, N. Liu, H. Wang, M. Vosgueritchian, Y. Yang, Y. Cui and Z. Bao, *Nano Lett.*, 2011, **11**, 4438-4442.
18 G. Yu, L. Hu, M. Vosgueritchian, H. Wang, X. Xie, J. R. McDonough, X. Cui, Y. Cui and Z. Bao, *Nano Lett.*, 2011, **11**, 2905-2911.
19 S. Yang, X. Song, P. Zhang and L. Gao, *ACS Appl. Mater. Interfaces*, 2013, **5**, 3317-3322.

View Article Online
DOI: 10.1039/C5RA05514H

20 Q. Li, X.-F. Lu, H. Xu, Y.-X. Tong and G.-R. Li, *ACS Appl. Mater. Interfaces*, 2014, **6**, 2726-2733.
21 A. L. M. Reddy, M. M. Shaijumon, S. R. Gowda and P. M. Ajayan, *J. Phys. Chem. C*, 2010, **114**, 658-663.
22 W. Chen, R. B. Rakhi, L. Hu, X. Xie, Y. Cui and H. N. Alshareef, *Nano Lett.*, 2011, **11**, 5165-5172.
23 A. Sumboja, C. Y. Foo, J. Yan, C. Yan, R. K. Gupta and P. S. Lee, *J. Mater. Chem.*, 2012, **22**, 23921-23928.
24 R. Ranjusha, K. M. Sajesh, S. Roshny, V. Lakshmi, P. Anjali, T. S. Sonia, A. S. Nair, K. R. V. Subramanian, S. V. Nair, K. P. Chennazhi and A. Balakrishnan, *Microporous Mesoporous Mater.*, 2014, **186**, 30-36.
25 M. Ghaffari, Y. Zhou, H. Xu, M. Lin, T. Y. Kim, R. S. Ruoff and Q. M. Zhang, *Adv. Mater.*, 2013, **25**, 4879-4885.
26 R. S. Kalubarme, H. S. Jadhav and C.-J. Park, *Electrochimica Acta*, 2013, **87**, 457-465.
27 Z.-S. Li, H.-Q. Wang, Y.-G. Huang, Q.-Y. Li, X.-Y. Wang, *Col. and Surf. A: Physicochem. Eng. Aspects*, 2010, **366**, 104-109.
28 T. M. Benedetti, F. F. C. Bazito, E. A. Ponzio and R. M. Torresi, *Langmuir*, 2008, **24**, 3602-3610.
29 P. C. Howlett, D. R. MacFarlane and A. F. Hollenkamp, *Electrochem. Solid-State Lett.*, 2004, **7(5)**, A97A101.
30 H. Sakaebe, H. Matsumoto and K. Tatsumi, *J. Power Sources*, 2005, **146**, 693-697.
31 H. Sakaebe and H. Matsumoto, *Electrochem. Commun.*, 2003, **5**, 594-598.
32 T. Sato, T. Maruo, S. Marukane and K. Takagi, *J. Power Sources*, 2004, **138**, 253-261.
33 K. Hayashi, Y. Nemoto, K. Akuto and Y. Sakurai, *J. Power Sources*, 2005, **146**, 689.
34 N. Byrne, P. C. Howlett, D. R. MacFarlane and M. Forsyth, *Adv. Mater.*, 2005, **17**, 2497-2501.
35 V. R. Koch, C. Nanjundiah, G. B. Appetecchi, B. Scrosati, *J. Electrochem. Soc.*, 1995, **142**, L116-L118.
36 H. Nakagawa, S. Izuchi, K. Kuwana, T. Nukuda and Y. Aihara, *J. Electrochem. Soc.*, 2003, **150**, A695-A700.
37 D. R. MacFarlane, P. Meakin, J. Sun, N. Amini and M. Forsyth, *J. Phys. Chem. B*, 1999, **103**, 4164-4170.
38 A. E. Visser, R. P. Swatlowski, W. M. Reichert, R. Mayton, S. Sheff, A. Wierzbicki, J. H. Davis and R. D. Rogers, Chem. Commun., 2001, 135-136.
39 D. Rochefort and A. L. Pont, *Electrochem. Commun.*, 2006, **8**, 1539-1543.
40 T. Nohira, T. Ishibashi and R. Hagiwara, *J. Power Sources*, 2012, **205**, 506-509.
41 T. Khoo, A. Somers, A. A. J. Torriero, D. R. MacFarlane, P. C. Howlett and M. Forsyth, *Electrochim. Acta*, 2013, **87**, 701-708.
42 P. Wang, Y. NuLi, J. Yang and Z. Feng, *Surf. Coat. Technol.*, 2006, **201**, 3783-3787.
43 N. Birbilis, P. C. Howlett, D. R. MacFarlane and M. Forsyth, *Surf. Coat. Technol.*, 2007, **201**, 4496-4504.
44 H.-Q. Wang, Z.-S. Li, Y.-G. Huang, Q.-Y. Li and X.-Y. Wang, *J. Mater. Chem.*, 2010, **20**, 3883-3889.
45 Y.-S. Li, I-W. Sun, J.-K. Chang, C.-J. Su and M.-T. Lee, *J. Mater. Chem.*, 2012, **22**, 6274-6279.
46 X. Li and B. Wei, *Nano Energy*, 2012, **1**, 479-487.
47 X. Zhang, D. Zhao, Y. Zhao, P. Tang, Y. Shen, C. Xu, H. Li and Y. Xiao, *J. Mater. Chem. A*, 2013, **1**, 3706-3712.
48 J.-K. Chang, M.-T. Lee, W.-T. Tsai, M.-J. Deng, H.-F. Cheng and I-W. Sun, *Langmuir*, 2009, **25(19)**, 11955-11960.
49 M. Zhi, C. Xiang, J. Li, M. Li and N. Wu, *Nanoscale*, 2013, **5**, 72-88.
50 M. Xu, L. Kong, W. Zhou, and H. Li, *J. Phys. Chem. C*, 2007, **111**, 19141-19147.
51 T.Y. Kim, G. Jung, S. Yoo, K. S. Suh and R. S. Ruoff, *ACS Nano*, 2013, **7(8)**, 6899-6905,.
52 P. Tamailarasan and S. Ramaprabhu, *J. Phys. Chem. C*, 2012, **116(27)**, 14179-14187.
53 C. Liu, Z. Yu, D. Neff, A. Zhamu and B. Z. Jang, *Nano Lett.*, 2010, **10(12)**, 4863-4868.
54 Y. Chena, X. Zhang, D. Zhang, P. Yu and Y. Ma, *Carbon*, 2011, **49**, 573-580.
55 T. Y. Kim, H. W. Lee, M. Stoller, D. R. Dreyer, C. W. Bielawski, R. S. Ruoff and K. S. Suh, *ACS Nano*, 2011, **5(1)**, 436-442.
56 W. Lu and R. Hartman, *J. Phys. Chem. Lett.*, 2011, **2(6)**, 655-660.
57 L. Zhang, F. Zhang, X. Yang, G. Long, Y. Wu, T. Zhang, K. Leng, Y. Huang, Y. Ma, A. Yu and Y. Chen, *Scientific Reports*, 2011, **3**, 1408.
58 K. Pinkert, M. Oschatz, L. Borchardt, M. Klose, M. Zier, W. Nickel, L. Giebeler, S. Oswald, S. Kaskel and J. Eckert, *ACS Appl. Mater. Interfaces*, 2014, **6(4)**, 2922-2928.
59 W.-W. Liu, X.-B. Yan, J.-W. Lang, J.-B. Pu and Q.-J. Xue, *New J. Chem.*, 2013, **37**, 2186-2195.
60 P. Umek, A. Gloter, M. Pregelj, R. Dominko, M. Jagodic, Z. Jaglicic, A. Zimina, M. Brzhezinskaya, A. Potocnik, C. Filipic, A. Levstik and D. Arcon, *J. Phys. Chem. C,* 2009, **113(33)**, 14798-803.
61 B. Yin, S. Zhang, H. Jiang, F. Qu and X. Wu, *J. Mater. Chem. A*, 2015, **3**, 5722-5729.
62 K. Chen, Y. D. Noh, K. Li, S. Komarneni and D. Xue, *J. Phys. Chem. C*, 2013, **117(20)**, 10770-10779.
63 J. K. Yuan, W. N. Li, G. Sinue and L. Steven, *J. Am. Chem. Soc.*, 2005, **127**, 14184-14185.
64 S. Maiti, A. Pramanik and S. Mahanty, *ACS Appl. Mater. Interfaces*, 2014, **6(13)**, 10754-10762.
65 S. Jana, S. Pande, A. K. Sinha, S. Sarkar, M. Pradhan, M. Basu, S. Saha and T. Pal, *J. Phys. Chem. C*, 2009, **113**, 1386-1392.
66 A. K. Sinha, M. Pradhan and T. Pal, *J. Phys. Chem. C*, 2013, **117**, 23976-23986.
67 D.-Y. Sung, I. Y. Kim, T. W. Kim, M.-S. Song and S.-J. Hwang, *J. Phys. Chem. C*, 2011, **115**, 13171-13179.
68 M. Xu, L. Kong, W. Zhou and H. Li, *J. Phys. Chem. C*, 2007, **111 (51)**, 19141-19147.
69 M. D. Stoller and R. S. Ruoff, *Energy Environ. Sci.*, 2010, **3**, 1294-1301.
70 T. Y. Kim, G. Jung, S. Yoo, K. S. Suh and R. S. Ruoff, *ACS Nano*, **8**, 2013, 6899-6905
71 H. Jiang, T. Zhao, J. Ma, C. Yan and C. Li, *Chem. Commun.*, 2011, **47**, 1264.
72 P. Simon and Y. Gogotsi, *Nat. Mater.*, 2008, **7**, 845-854
73 A. J. R. Rennie, N. Sanchez-Ramirez, R. M. Torresi and P. J. Hall, *J. Phys. Chem. Lett.*, 2013, **4 (17)**, 2970-2974.
74 J. Gamby, P. L. Taberna, P. Simon, J. F. Fauvarque and M. Chesneau, *J. Power Sources*, 2001, **101**, 109-116.
75 M. Toupin, D. Belanger, I. R. Hill and D. Quinn, *J. Power Sources*, 2005, **140**, 203-210.
76 Z. Xu, Z. Li, C. M. B. Holt, X. Tan, H. Wang, B. S. Amirkhiz, T. Stephenson and D. Mitlin, *J. Phys. Chem. Lett.*, 2012, **3(20)**, 2928-2933
77 M. Hughes, G.Z. Chen, M.S.P. Shaffer, D.J. Fray and A. H. Windle, *Chem. Mater.*, 2002, **14(4)**, 1610-1613.
78 S. Zhang, C. Peng, K. C. Ng, and G. Z. Chen, *Electrochimica Acta*, 2010, **55**, 7447-7453.
79 S.-B. Yoon, J.-P. Jegal, K. C. Roh and K.-B. Kim, *J. Electrochem. Soc.*, 2014, **161(4)**, H207-H213.

View Article Online
DOI: 10.1039/C5RA05514H

Table of Contents Entry

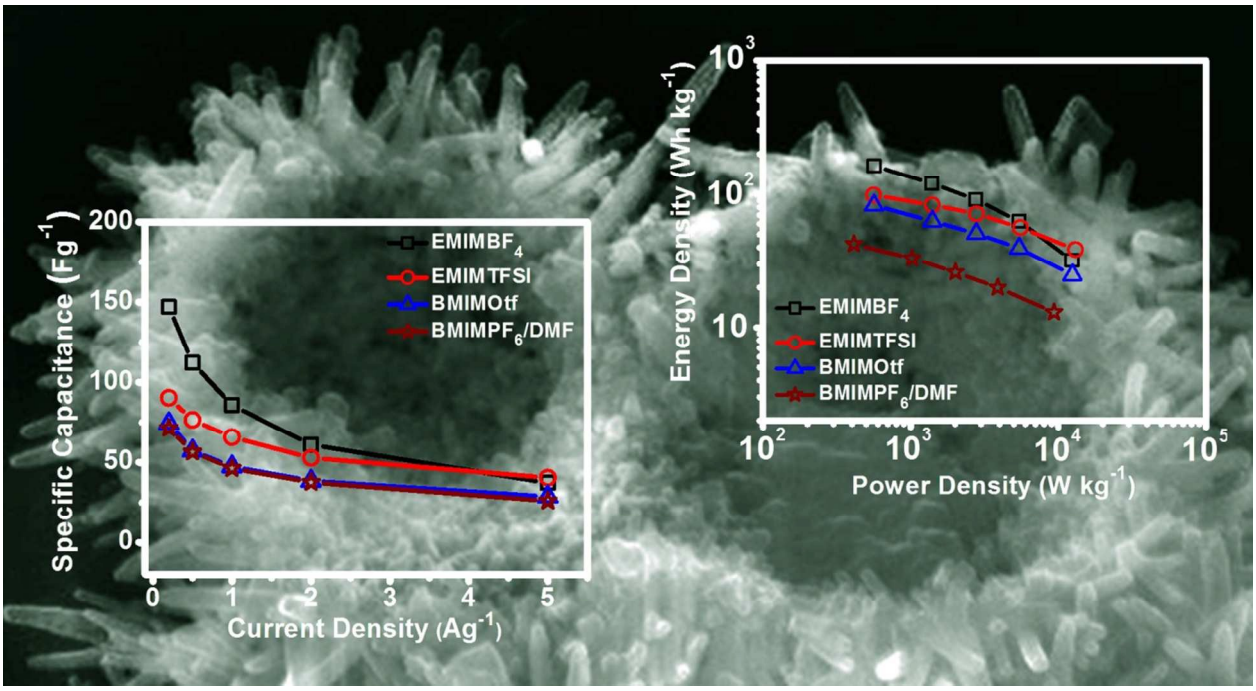

Activated carbon //MnO_2 hollow sphere asymmetric supercapacitor shows an energy density of 163 $Wh.Kg^{-1}$ in $EMIMBF_4$ ionic liquid as electrolyte.